The effect of inelastic deformation on crack loading

DIMOSTHENIS FLOROS

Cover:
Distribution of the plastic strain component $\epsilon_{11}^{\mathrm{p}}$ over a single edge-cracked specimen, computed by local constitutive theory (left) and by gradient-enhanced constitutive theory for finite value of the internal length scale (right).

The effect of inelastic deformation on crack loading
Thesis for the degree of Licentiate of Engineering in Solid and Structural Mechanics
DIMOSTHENIS FLOROS
Department of Applied Mechanics
Chalmers University of Technology

Abstract

Rolling contact fatigue (RCF) cracks in rails are among the most detrimental railway track defects, in relation to reliability and cost. The cracks grow in a mixed mode II & III, which in combination with the rotating stress field in the neighborhood of the crack-tip, large plastic deformations on the rail surface, crack face friction due to the compressive stresses from the wheel load and anisotropic crack growth resistance, add to the complexity related to the study of RCF cracks. In contrast, most existing criteria for RCF crack propagation in the literature feature quantities that are susceptible to limitations, such as small scale yielding (see e.g. stress intensity factors), pure mode I growth, unloaded crack faces. Consequently, the range of validity (and precision) of existing criteria may be questioned.

The current work focuses on one of the complicating factors: the role of inelastic deformation on the crack loading. At the first part, a qualitative assessment is performed of the mechanisms that accompany elastoplastic deformations of multi-axially loaded cracks. For this purpose, numerical simulations are carried out in pre-cracked tubular specimens subjected to torsional and axial loading in various load configurations. Elastoplastic deformations are quantified here via the relative deformation of initially aligned crack faces, here denoted as crack face displacement. The range of the crack face displacement over each load cycle accounts for the severity of the crack situation (in a manner analogous to the range of the stress intensity factor). Results are identified as shakedown and ratcheting effects and compared to experimental trends in literature.

The work continues with the study of configurational (or material) forces for gradient-enhanced inelasticity. The severity of the crack loading is here measured via energy release rates (a generalization of the J-integral for inelasticity with material dissipation), which stem from the computed material forces. The mesh sensitivity of the energy release rates is investigated for the cases of a smooth interface and an embedded discrete singularity. Results highlight that the proposed gradient-regularized scheme provides sufficient regularity for the computation of material forces. Obtaining a rather mesh insensitive material force field for inelasticity, is considered a necessary step towards the development of a criterion for RCF crack propagation based on material forces.

Keywords: Numerical simulation, Mixed mode, Configurational mechanics, Gradient plasticity.

To my parents, Theodoros and Giannoula Floros

PREFACE

The ongoing work in this thesis is part of CHARMEC center of excellence in railway mechanics, Applied Mechanics Department, Chalmers University of Technology, Gothenburg, Sweden. The research performed within the project is supported financially and in-kind by Trafikverket and voestalpine Schienen, for which they are gratefully acknowledged.

The work in this thesis so far would not be possible to accomplish without the contribution of my supervisors. Specifically, I would like to thank prof. Kenneth Runesson for his generous sharing of his multi-physics knowledge during meetings and the inspiration he has transpired to me the last few years. Special thanks I owe to prof. Anders Ekberg. His input regarding all aspects of the project and especially during the preparation of paper A was invaluable, as is his availability during all possible hours during the day. Last but not least, I would like to acknowledge my main supervisor, prof. Fredrik Larsson. He has been a great support and an endless source for demystifying computational mechanics the last three or more years. I am looking forward to working with all of you for at least two more years!

To continue with the people in my immediate working environment, I would like to thank all the "usual suspects", i.e. the colleagues/friends who tend to stay at work a little bit later than the "normal" working hours. We have been sharing endless moments of laughter, joy, as well as agony and hope regarding our research and those simulations that "never converge".

To this end, words are not enough to describe my gratitude to my family, my parents Theodoros and Giannoula Floros, who have sacrificed all about their personal lives, in order for me to have to think only about my education, once they have everything else taken care for me. Finally, my uncle Major General Dimosthenis Floros is also gratefully acknowledged for his inspiration and support throughout my academic career so far.

Gothenburg, 2016
Dimosthenis Floros

Thesis

This thesis consists of an extended summary and the following appended papers:

Paper A D. Floros, A. Ekberg, and K. Runesson. A numerical investigation of elastoplastic deformation of cracks in tubular specimens subjected to combined torsional and axial loading. *International Journal of Fatigue* (2016). ISSN: 0142-1123

Paper B D. Floros, F. Larsson, and K. Runesson. On configurational forces for gradient-enhanced inelasticity. *To be submitted for international publication* (2016)

The appended papers have been prepared in collaboration with the co-authors. The author of this thesis was the main responsible for the progress of the work. Namely, took part in planning of the papers and the development of the theory, carried out numerical implementation and simulations, and wrote major parts of the papers.

CONTENTS

Part I
Extended Summary

1   Introduction

1.1   Motivation for research and background

Among railway track surface defects, *head checks* are considered one of the most detrimental in terms of reliability and cost. These are small, parallel cracks, inclined to the running direction, that appear at the gauge corner of the high rail in curves, see Fig 1.1. Head checks are *rolling contact fatigue* (RCF) phenomena. RCF cracks stem from preexisting internal or surface defects in the rail material that tend to propagate under the action of the frictional rolling contact due to the passage of trains. The severity of the load situation may be better viewed considering that the wheel–rail contact patch is similar in size to that of a small coin, see Marshall et al. [3]. The maximum static axle load, which is carried on two such surfaces, is to-date as high as 30 t, with extreme cases up to and above 42 t, see Girsch et al. [4].

Figure 1.1: *Periodic formation of RCF cracks at the gauge corner of a railway track.*

Regarding growth of head checks with time, there are two prominent scenarios: after an initial stage of low-angled, with respect to the rail surface, growth, the rolling contact fatigue cracks either grow upwards causing spalling of the railway material, or alternatively, shift downwards, transversely to the longitudinal axis of the rail, resulting in complete local failure of the rail, see Fig. 2.1. Both scenarios induce reliability issues in the railway operation. They also lead to environmental effects and large maintenance costs, see Magel [5]. To prevent and mitigate these issues, the need for *accurate prediction of the direction and the rate of crack propagation* is vital.

Crack growth, of the kind that appears in rails, is a complex phenomenon which is not fully understood, nor handled in the current literature. Currently, there exist only limited methods for the prediction of the remaining service life of cracked components subjected to RCF. The same limitation holds when it comes to quantifying the severity of existing cracks based on the crack morphology. The majority of the existing methods in literature are based on quantities susceptible to specific limitations. For example, the use of stress intensity factors (SIFs) is limited to small scale yielding (cf. the large plastic deformations at the rail surface and the crack-tip in RCF), see Dowling [6]. Further, criteria based on SIFs have limitations in predicting crack growth under complete crack closure (cf. large compressive stress from the passage of wheels over the crack mouth). Another quantity used in RCF crack propagation criteria is the crack-tip opening displacement (CTOD). This quantity, although it overcomes most of the limitations regarding e.g. SIF, is "directly" related to crack growth with a Paris type relation only under small scale yielding conditions.

The primary goal of the current project is *to investigate via numerical simulations, the growth rate and crack growth direction of surface cracks in the rail head*. Advances towards this goal are expected to contribute to the optimization of the maintenance process of railway tracks in terms of more targeted inspection intervals, reduced disturbance of traffic for maintenance work and more efficient use of resources, by avoiding premature replacement/removal of railway steel material, component-wise or through grinding.

At the first part, the effect of load multi-axiality on inelastic deformation of cracks is investigated, see Section 3 and Floros et al. [1] (paper A). Numerical simulations are performed on pre-cracked tubular specimens subjected to various configurations of torsional and axial loads. Elastic–plastic deformations are quantified by the relative displacement of initially aligned crack faces, termed here as crack face displacements. The range of crack face displacements is taken here to reflect the severity of the crack loading, in a manner analogous to how the range of SIFs traditionally is employed, see Tanaka [7]. Identified *ratcheting* effects in crack face displacement indicate *crack blunting* and/or kinking, while *shakedown* effects are found to relate to the build-up of residual stresses. Results aid in the interpretation of experimental results and in design of future experiments.

In accordance with the preceeding discussion, a criterion for RCF crack propagation should be able to capture the direction and rate of growth. One way to view the rate of growth is via the rate of a crack driving potential, see e.g. Brouzoulis and Ekh [8]. The respective potential may, in principle, be comprised of the difference between the measure that drives the growth and the respective measure that resists it, the latter being for instance a material property such as the critical strain energy release rate G_c, see Griffith [9]. The second part of the current thesis pertains to the establishment of a thermodynamically consistent crack driving force based on configurational forces, that is computable, i.e. does not exhibit "pathological" mesh sensitivity.

In view of the numerical issues encountered in literature regarding the computation of configurational forces-based crack driving force for inelasticity (see e.g. Näser et al. [10] and Tillberg et al. [11]), a gradient-regularized variational formulation is proposed in Floros et al. [2] (paper B). With the aid of this formulation, two goals are accomplished. First, nodal values of the gradient fields are obtained already from the primary (direct

motion) problem. Thus no nodal smoothing of internal variables from known values at integration points is required at the post-processing. According to e.g. Tillberg et al. [11], the discretization error arising from related nodal smoothing techniques comprises one of the numerical issues mentioned above. Secondly, the proposed gradient-enhanced formulation provides sufficient regularity for the computation of the material dissipation[1] part of the crack driving force.

1.2 Purpose

The aim of the thesis is twofold. The first objective is to investigate the influence of mixed mode loading on the elastic–plastic deformation of cracks. It relates to a qualitative analysis of how the crack loading (as quantified by crack face displacements) is affected by various configurations of combined torsional and axial loading, see Floros et al. [1] (Paper A).

The second aim is the development of a reliable measure for the quantification of crack loading. The employed measure is based on configurational (or material) forces for inelasticity, see Floros et al. [2] (paper B). The derived measure may, at a later stage, be used to establish the crack driving potential in a criterion for crack propagation.

1.3 Limitations

According to the preceding discussion, two challenges need to be addressed by the candidate crack growth criteria. Namely, the prediction of direction and rate of crack propagation. Although both are required in a holistic view, the present work focuses mostly on deriving quantities to predict the crack growth rate, presuming a known crack path (or orientation). It should in this context be noted that only stationary cracks are treated in the current thesis.

In addition, the study of RCF cracks on the rail surface has, at the final stage, to be able to account for the 3D morphology of such cracks. This requirement stems from the 3D morphology of operational RCF cracks, where the fracture surfaces extend also transversely to the crack propagation plane. In Fig. 1.2, the surfaces of an RCF crack are depicted, as obtained from 3D reconstruction (colored) and metallography (mesh). In Floros et al. [1], the mixed mode fatigue behavior of a thin-walled specimen is examined via 3D FE-analysis, featuring cracks with initially plane fracture surfaces. With the progressing of the applied cyclic loads, out-of-plane deformations also take place, however, they are not analyzed due to the low resolution of the FE-model in the thickness direction.

The surface layer of the rail exhibits large plastic deformations which significantly alter the material characteristics. As a consequence, an anisotropic layer is formed at the top of the rail, see Larijani et al. [13]. In the general case, this implies the formation of anisotropic

---

[1]In Runesson et al. [12], it is shown that the total configurational force may be split in the configurational and the material dissipation part. The former is considered mesh-insensitive, provided that certain requirements are fulfilled, see e.g. Näser et al. [10]. Thus the mesh sensitivity in the total configurational force is attributed mainly to the material dissipation part, see e.g. Tillberg et al. [11].
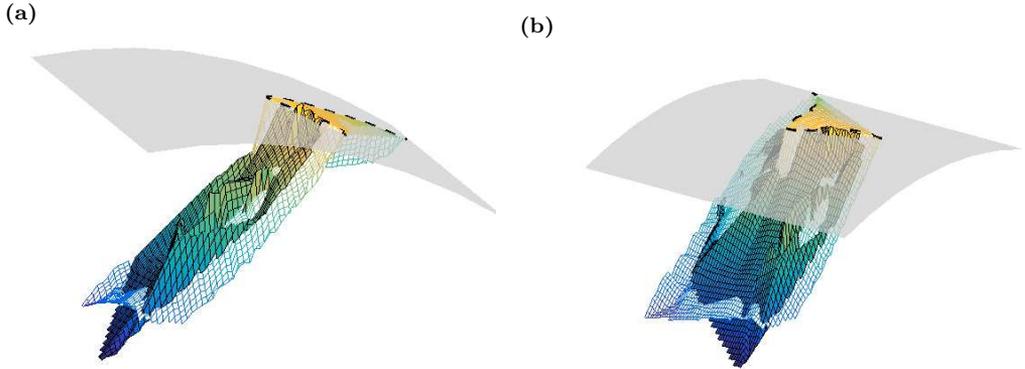
Figure 1.2: *RCF crack morphology, as obtained from 3D reconstruction in the lab (colored areas) and metallography (mesh). (a) Side view. (b) Front view. (image with courtesy of Casey Jessop, CHARMEC project "Damage in wheel and rail materials").*

crack growth resistance. As discussed in Section 1.1, crack growth resistance comprises one of the constituents that define the crack driving potential in a crack propagation criterion. Therefore, the significance of anisotropy in crack growth resistance pertinent to the current study is noted. In both papers this thesis is comprised of, only isotropic material behavior is examined.

The effect of crack face friction, which becomes more pronounced under the large compressive stresses from the passage of the trains, has substantial influence on crack growth characteristics, see e.g. Bower [14]. In Floros et al. [1], friction-less contact is assumed between the crack faces. In Floros et al. [2], only the corresponding internal part of the configurational forces is studied, thereby the configurational forces acting at the crack surfaces are omitted due to added complexity even for the case of hyperelasticity, see Brouzoulis and Ekh [8].

2 Fatigue behavior of fractured specimens under mixed mode loading

2.1 Characteristics of mixed mode crack propagation

Mixed mode crack growth occurs frequently in components subjected to combined axial and torsional load, see e.g. Fonte and De Freitas [15]. In comparison to crack initiation under multi-axial loading conditions which is a relatively well-investigated phenomenon, see Papadopoulos [16], the mechanisms behind mixed mode crack growth have received less attention, even though the situation has improved during the last decades, see Fatemi and Shamsaei [17].

There exists a substantial number of experimental work in literature devoted to the effect of static torsion on solid, notched, pre-cracked, round bars subjected to cyclic axial

loading, see Fonte et al. [18], De Freitas et al. [19], Yang et al. [20]. Similar conclusions are drawn in all the aforementioned references: (a) a static torque decreases crack growth rates significantly compared to the case of pure cyclic axial load (of essentially the same load magnitude), (b) inclined ridges in 45° with respect to the crack growth plane are commonly found. Crack closure phenomena due to interlocking of the ridged fracture surfaces and increased plastic zone size at the crack-tip induced by the added static torsion are the mechanisms presumed to govern the decrease in crack growth rates, see also Brown et al. [21].

The formation of inclined ridges is explained in Hourlier and Pineau [22], as the continuous adjustment of the crack to the rotating principal stress directions due to the torsional load. The crack breaks into "partial fronts", as a result of this adjustment. A model for the mechanism behind the formation of such fracture surfaces is described in Zhizhong et al. [23].

In contrast to the previous load case, a somewhat more involved discussion is raised regarding the effect of static tension on specimens subjected to cyclic torsion. In Brown et al. [21], the application of static tension up to some $2\,\mathrm{kN}$ combined with cyclic torsion, results in ten times higher crack growth rates than for pure torsion. In Tschegg et al. [24], it is shown that static tension superimposed on cyclic mode III, results in increased "true" mode III[1] crack growth rates. This effect is more pronounced for increasing magnitude of static tension, until a value of $K_{\mathrm{I}} = 9\,\mathrm{MPa}\sqrt{\mathrm{m}}$. The increase is attributed to the suppression of the crack closure effects that accompany mode III crack growth, by the superimposed static tension that "opens" the crack. In contrast, Ritchie et al. [25] report that the addition of static tension of some $K_{\mathrm{I}} = 60\,\mathrm{MPa}\sqrt{\mathrm{m}}$ on top of cyclic torsion, did not result in increase in measured crack growth rates. The discrepancy in the effect of static tension is discussed in Tschegg and Stanzl [26].

In addition, inclined ridges ("factory-roof" fracture surface) are also found to form for the case of cyclic torsion superimposed on static tension, see Brown et al. [21]. As is also the case for combined cyclic axial and static torsional load, such growth is clearly a deviation into mode I growth (along the rotating principal stress plane). However, for higher values of cyclic torque, it is reported that mode III growth is observed (radially growing cracks), as evident by the occurence of "smooth" fracture surfaces (rubbing of fracture surfaces). In summary, for the examined fracture cases, low cyclic torque is reported to result in mode I growth (ΔK_{I}). The transition to mode III type of growth (ΔK_{III}) is estimated by Brown et al. [21] to take place when the ratio $\Delta K_{\mathrm{III}}/\Delta K_{\mathrm{I}} \approx 0.67$, assuming that: (a) Pineau's criterion that cracks eventually grow in the direction that results in the highest crack growth rate is true, see Section 2.2.1, and, (b) linear elastic fracture mechanics (LEFM) can still be used (with caution) for the high applied torques, which result in large plastic zone sizes and thereby a violation of the small scale yielding requirement.

---

[1]In Tschegg et al. [24], the term "true" crack growth rate comprises a way to "remove" from the measured growth rates, the effect of crack face friction, thereby resulting in higher crack growth rates.

2.1.1 RCF crack propagation in rails

RCF cracks in rails grow initially in mixed mode II & III, at a shallow angle to the rail surface. Low-angled growth continues until a critical length, where cracks may branch either upwards–causing spalling of the rail material–or, downwards–causing complete local failure of the rail–see Fig. 2.1. An overview of factors that influence RCF surface and subsurface crack initiation and propagation in both rails and wheels can be found in Ekberg and Kabo [27]. Influencing factors of "short" RCF crack propagation are discussed in Ringsberg and Bergkvist [28]. In the latter work, the limits in which (elastoplastic fracture mechanics) EPFM or LEFM is applicable are also discussed and examined numerically. It is especially noted that for "short" inclined surface initiated cracks, those limits are not well-defined.
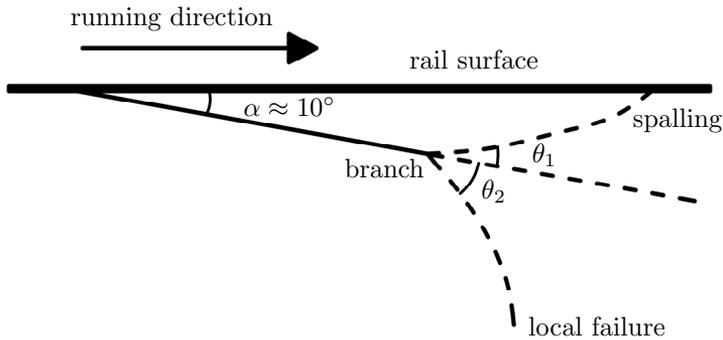
Figure 2.1: *RCF crack propagation direction(s).*

2.2 Analysis of multi-axial fatigue behavior of fractured ductile specimens

2.2.1 A short review of crack propagation criteria under mixed mode loading with applications on RCF

In Erdogan and Sih [29], the *maximum tangential stress criterion* is derived and tested, on the brittle fracture of linear elastic plates. According to this criterion, cracks grow perpendicular to the direction of maximum tangential stress σ_θ. This criterion, as well as the *criterion of maximum shear stress* are used in Otsuka et al. [30] to derive the stress intensity factors K_σ and K_τ, respectively. The ranges formed by the latter quantities may be used in Paris type models for the prediction of crack growth rates, see Bold et al. [31], Bower [14]. The potential use of such criteria in RCF is indicated in Fig. 2.2. In Wong et al. [32], the loading conditions present during RCF crack branching are experimentally examined, and an empirical branch criterion is proposed, based on the degree of overlap between the applied modes and the range of the effective SIF in mode I, ΔK_{Ieff}.

Based on experiments on pre-cracked notched round bars subjected to cyclic axial
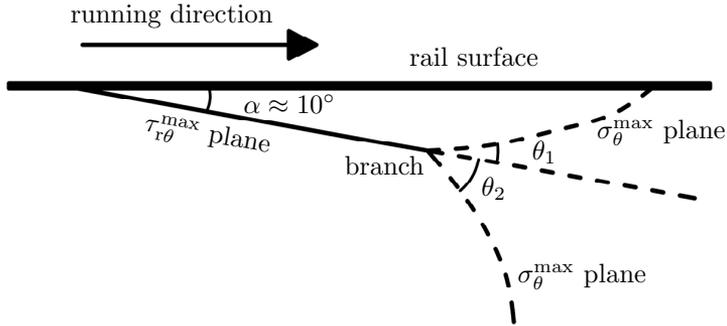
Figure 2.2: *"Rough" estimation of RCF crack propagation direction(s) based on criteria proposed in Erdogan and Sih [29].*

and static torsional load, in Hourlier and Pineau [22] it is motivated that fatigue crack propagation takes place in the direction that maximizes the fatigue crack growth rate da/dN. *Pineau's criterion* is frequently employed in comparisons between predictive models and experimental crack growth curves, as well as in numerical simulation of e.g. RCF crack propagation, see Bogdański and Brown [33].

According to the *minimum strain energy density criterion*, as derived in Sih [34], cracks grow in the direction that minimizes the strain energy. The pertinent theory is employed in Chue and Chung [35] along with 2D FE simulations, in order to predict pitting formation caused by surface cracks.

As a concluding remark, it is noted that (all) criteria currently available in literature are able to capture growth under conditions which are predominantly mode I. The challenges regarding RCF conditions are summarized as follows: (a) there exists no consensus to-date on how to account for mode mixity in an appropriate manner, (b) crack face friction, which commonly occurs in mixed mode loading, is difficult to quantify in theoretical models and experiments, (c) crack closure effects, interlinked with crack face friction, are also hard to account for, (d) the effect of lubrication (related to crack face friction) adds even more complexity, (e) residual stresses appear to strongly affect crack growth and may act in favor of preferred directions of growth in mixed mode loading conditions.

2.2.2 Quantification of elastic–plastic response of fractured ductile specimens

Traditionally, the loading of a crack is quantified by the stress intensity factor(s). These relate to LEFM conditions, which makes them only valid under conditions of: (a) small-scale yielding, such that *regions of K-dominance* are still applicable (see Dowling [6]), (b) sufficiently long cracks compared to the material microstructure. Thus, for short cracks embedded in severely deformed plastic layers (like incipient RCF cracks), stress intensity factors are not suitable. In the presence of large plastic deformations, a quantification using strain intensity factors improves the correlation with experimental crack growth

curves, see Brown et al. [21].

In relation to the stress intensity factors, mixed mode loading is often quantified by equivalent ranges of stress intensity factors. This implies a (non-linear) combination of the modes present in the considered fracture case, see Tanaka [7]. In turn, the equivalent range enters a Paris type model for crack propagation. In this context, effects such as crack closure and friction are modeled by e.g. scaling the nominal ranges of stress intensity factors ΔK_{nom}, by factors such as the crack closure ratio and the crack sliding displacement, see Wong et al. [32]. Extrapolating to "true" crack growth rates at zero crack length is another example of how to account for crack closure effects, see Tschegg [36].

To overcome the small scale yielding limitations applicable to stress intensity factors, the range of CTOD or crack-tip shear displacement (CTSD) is often employed, see e.g. Tschegg et al. [24]. However, in the general inelastic case, there exists no closed-form relation between the CTOD and the stress intensity factors (or the J-integral), as is the case under elastic conditions, see Suresh [37]. Another ambiguity regarding the CTOD is the relative nature of the pertinent quantity, since there is no consensus on how far away from the crack-tip, CTOD should be measured. This may suggest that the CTOD could serve more as a qualitative measure, rather than quantitative, see Floros et al. [1]. In contrast to SIFs: (a) crack closure effects are explicitly taken into account in CTOD, (b) even for mixed mode load cases, the individual contribution of each mode into the total displacement in the near-tip region can be accounted for, explicitly. An example of how to account for mixed mode crack growth with the CTOD and CTSD is with the vector crack-tip displacement (CTD), see Li [38].

A quantity of prominent importance for the quantification of the crack loading in EPFM is the path-independent J-integral, see Rice [39]. It is a scalar quantity that reflects the energy release rate due to unit crack advance in the tangential to the crack-tip direction. In fracture cases with large plastic deformations under cyclic loading, even the very definition of this quantity is under question, since non-linear elastic response is assumed for proving path-independence (through the assumption $\boldsymbol{\sigma} \stackrel{\mathrm{def}}{=} \partial\psi/\partial\boldsymbol{\epsilon}$), see Rice [39]. An example of the use of the J-integral as a measure to quantify mixed mode crack loading is described in Hoshide and Socie [40].

In a more generic framework, configurational (or material) forces are also used for the analysis of the fatigue behavior of fractured specimens. These can be seen as forces "acting" on the undeformed configuration (as opposed to classical Newtonian forces acting on the current configuration). The advantages of forming the configurational motion problem in terms of a vectorial quantity such as the material forces, as opposed to scalar quantities such as the J-integral, are described in Steinmann [41].

In numerical simulations, configurational forces are classically computed based on "conventional" displacement-based formulations, using standard shape functions. In elastic–plastic simulations, depending on the employed definition of material forces, this approach results in "pathological" mesh dependence, see Tillberg et al. [11]. Another approach is the use of mixed variational formulation in terms of the displacements and the internal variables field, see Menzel et al. [42]. In Floros et al. [2], configurational forces are computed for a gradient-regularized mixed variational formulation in terms of the displacements and the micro-traction. The latter quantity is defined in e.g. Gurtin [43].

2.2.3   Numerical methods

The combination of linear elastic FE-analysis and LEFM is very common in literature, for the modeling of the multi-axial fatigue behavior of fractured specimens. Linear elastic FE-analysis is used especially for the determination of stress intensity factors, which are then employed for the fatigue analysis of fractured continua. In Fonte and Freitas [44], the stress intensity factors for semi-elliptical surface cracks in round specimens under bending and torsion are determined by 3D FE-analysis. The authors report significant K_{II} for the torsional load, at the intercepting points between the vertices of the crack mouth and the free surface of the bar. This may be linked to the discussion on the crack kinking in Section 3.2. However, analysis of load cases involving torsion in pre-cracked round specimens by stress intensity factors should be performed with caution, due to the large plastic zone sizes at the crack front induced by torsion, see e.g. Fonte et al. [18].

In cases where LEFM does not suffice (for example, by violation of the small scale yielding requirement), elastic–plastic FE simulations may be used, in combination with EPFM. In Brown et al. [21], strain intensity factors are used to correlate fatigue crack growth data at notched, pre-cracked, round bars subjected to alternating torsion and static tension. For the determination of the strain intensity factors, the size of the plastic zone sizes ahead of the notch and the crack-tip are required, which are determined by elastic–plastic 2D FE-simulations.

The boundary element method (BEM) is also employed for (most often linear elastic) analysis of the multi-axial fatigue behavior of fractured specimens. The main advantage of BEM compared to volume-discretization methods (FEM) is that with the former, only the boundaries of a considered domain need to be discretized. In Citarella et al. [45], the dual boundary element method (DBEM) is used in the propagating crack 3D models of round solid bars under combined in-phase tension/torsion. The numerical results are compared to experiments, which show decreased fatigue lives for the combined load case, contrasted to pure cyclic Mode I.

More advanced modeling techniques are used for the analysis of the multi-axial fatigue behavior of ductile specimens. One such method is the extended finite element method, see Xu and Yuan [46].

3   Elastic–plastic crack deformation under axial and torsional load

3.1   Numerical model description

In Floros et al. [1] (paper A), the influence of a combined axial and torsional load on the elastic–plastic deformation of cracks is investigated. For that purpose, an FE-model of a thin-walled tubular specimen with a centric hole is developed, in the commercial FE-code Abaqus [47], see Fig. 3.1. The tube is sufficiently long such that no boundary effects are imposed from the prescribed loads and the fixed boundary conditions, at the ends of the tube. The diameter of the centric hole is small compared to the outer diameter of the

tube in order to effectively simulate an "infinite" plate under plane stress conditions, i.e. suppressing any 3D effects. Cracks emanating from the centric hole in circumferential and 45° inclined directions are studied.
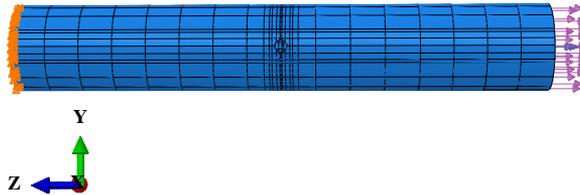
Figure 3.1: *Boundary conditions and applied loads.*

The structured FE-mesh consists of second-order hexahedral elements with 3 degrees-of-freedom per node, see Fig. 3.2a. Full integration over the element volume is performed. The mesh is graded towards the crack-tip such that the steep gradients are adequately resolved, see Fig. 3.2b.

(a)

(b)
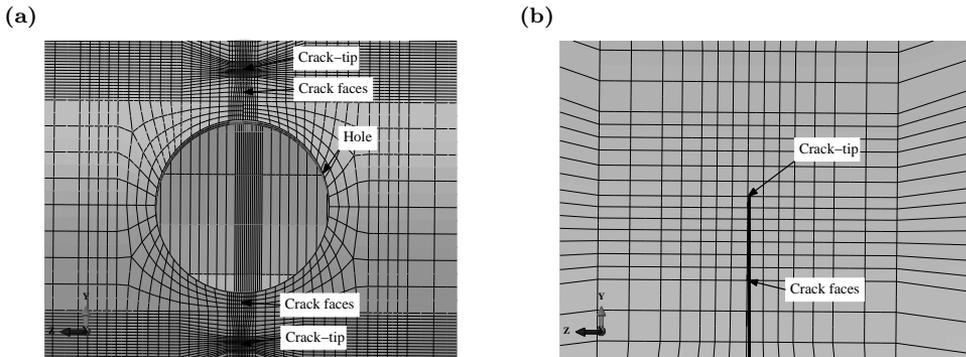
Figure 3.2: *(a) Structured mesh at circumferential cracks emanating from the hole. (b) Fine mesh near the crack–tip.*

An elastic–perfectly plastic material is initially employed. Some load cases are also investigated using a constitutive model featuring combined isotropic and non-linear kinematic hardening. Similar trends in terms of crack face displacements and the respective ranges are obtained for both material models, whereas the term crack face displacement and the range of this quantity are defined in Section 3.2.

3.2 Measured quantities, load cases and example results

The elastic–plastic deformation in this study is measured by the relative displacement δ in mode I & II, of initially aligned node-pairs at the two crack faces, see Fig. 3.3a. The range

of crack face displacement $\Delta\delta$ in mode I & II over each load cycle is used to quantify the crack loading, see Fig. 3.3b. Results are shown for node-pair 5, some 25 µm away from the crack-tip.
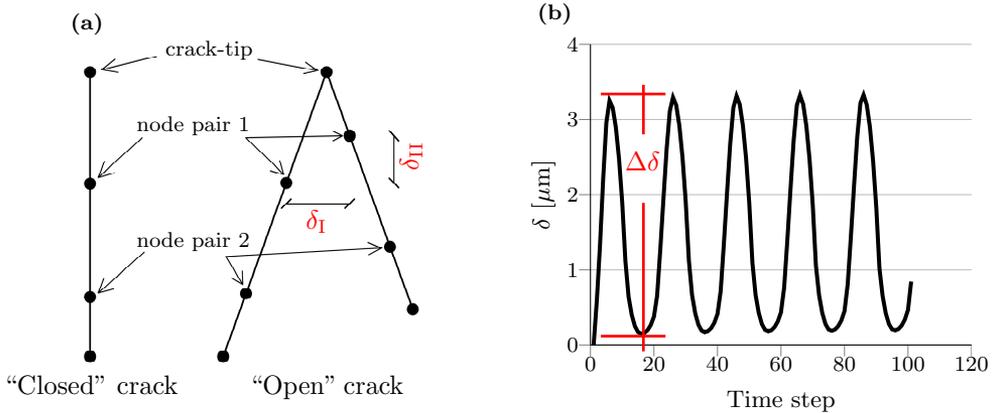
Figure 3.3: *(a) Definition of node pairs and crack face displacements, δ . (b) Definition of crack face displacement range $\Delta\delta$.*

The tube is subjected to combined stresses at the right end, as shown in Fig. 3.1. The respective load cases are described in Table 3.1.

Load case	Shear stress	Axial stress
1	-	Alternating $\sigma_a = \pm 144\,\text{MPa}$
2	Alternating $\tau_a = \pm 144\,\text{MPa}$	–
3	Static, $\tau = 144$ MPa	Alternating $\sigma_a = \pm 144\,\text{MPa}$
4	Alternating $\tau_a = \pm 144\,\text{MPa}$	Static, $\sigma = 144\,\text{MPa}$
5	Alternating $\tau_a = \pm 144\,\text{MPa}$	Alternating $\sigma_a = \pm 144\,\text{MPa}$

Table 3.1: Employed load cases and applied stress magnitudes.

Ranges of crack face displacements for the circumferential cracks featuring an elastic–plastic material response are shown in Fig. 3.4. Comparing the response for alternating axial load on top of static torsion (load case 3), with pure alternating axial load (load case 1), higher magnitudes in the respective ranges in both modes I & II are reported for the former case. However, pronounced progressive *shakedown* is observed for load case 3, while *shakedown* has occurred from load cycle 1 in load case 1. This trend may be linked to experimental results regarding the aforementioned load cases, where a significant decrease in crack growth rates is reported for load case 3, see e.g. Fonte et al. [18], De Freitas et al. [19].

In addition, for the combined cyclic axial/static torsional load case in literature, inclined ridges are found to form at the fracture surfaces ("factory-roof" shape), see Hourlier and Pineau [22], Fonte et al. [18]. The onset of this microscopic phenomenon is linked to the "kink" forming at the crack-tip. The respective deformation pattern is
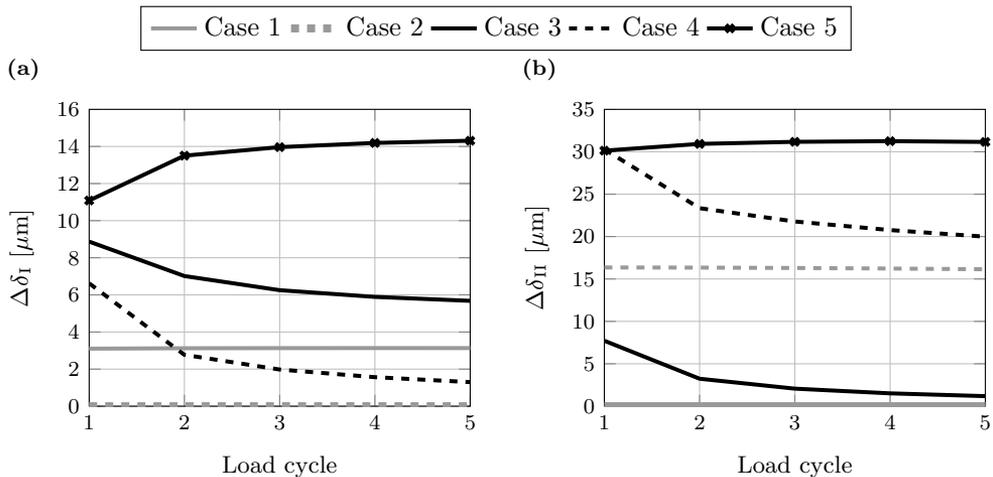
Figure 3.4: *Range of elastic–plastic crack face displacements for node pair 5 (for circum-ferential cracks). (a) $\Delta\delta_{\mathrm{I}}$ (mode I). (b) $\Delta\delta_{\mathrm{II}}$ (mode II).*

captured in FE-simulations, see e.g. Fig. 3.5a (Floros et al. [1]) and Fonte et al. [18] (cf. crack blunting forming for the same load case in the models with inclined cracks, see Fig. 3.5b).

Further discussions on all the load cases mentioned in Table 3.1 are found in Floros et al. [1].
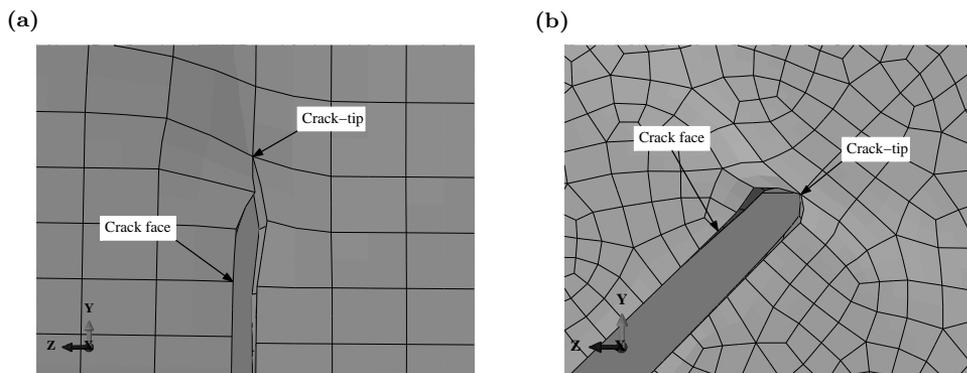
Figure 3.5: *Crack deformation under combined static torsion/alternating axial load at maximum tensile applied stress. (a) Circumferential cracks. (b) Inclined cracks.*

12

4 Computation of configurational forces based on a gradient-enhanced mixed formulation

4.1 Preliminaries

In Tillberg et al. [11], it is shown that the computation of material forces for (local) inelasticity is sensitive to the chosen FE-mesh size in problems involving discrete singularities, see also Näser et al. [10]. Two of the reasons that have been identified as causes for this sensitivity are: (a) the discretization error arising from the nodal smoothing techniques applied to the internal variables field obtained from "conventional" displacement-based variational formulations. It is reminded that in such formulations, values of the internal variables are known only at the integration points, thereby nodal smoothing is required at the post-processing for the subsequent evaluation of the spatial gradient of the internal variables, (b) the steep gradient fields close to the crack-tip that cannot be adequately resolved by the derivatives of standard (polynomial) shape functions. Additional reasons that have not been adequately investigated in literature are mentioned in Section 5.2.

To this end, the primary aim in Floros et al. [2] (paper B) is to derive a configurational forces field for inelasticity that is computable. This is attempted here in a coupled way: (a) gradient effects are taken into account in the constitutive setting, thus contributing in smoothing the steep gradients mentioned above, (b) a mixed variational formulation is constructed in terms of the displacements and a gradient field, the latter being the stress measure which is energy-conjugated to the spatial gradient of the internal variables. This, provides a continuous approximation of the gradient field after numerical solution of the proposed mixed variational formulation. With the nodal values of the pertinent field at hand, no nodal smoothing of internal variables is required at the post-processing.

4.2 Primary problem

As already mentioned in Section 4.1, a gradient-enhanced constitutive theory is chosen for the primary problem. Accounting for gradient effects, the free energy of a dissipative material (in small strains setting) reads

$$\psi(\boldsymbol{\epsilon}, \underline{k}, \underline{\boldsymbol{g}}) = \psi^{\mathrm{loc}}(\boldsymbol{\epsilon}, \underline{k}) + \psi^{\mathrm{gra}}(\underline{\boldsymbol{g}}), \tag{4.1}$$

where the strain field $\boldsymbol{\epsilon}(\boldsymbol{x}, t) = [\boldsymbol{u} \otimes \boldsymbol{\nabla}]^{\mathrm{sym}}$, the internal variables field $\underline{k}(\boldsymbol{x}, t)$, and the spatial gradient of $\underline{k}$, i.e. $\underline{\boldsymbol{g}}(\boldsymbol{x}, t) \stackrel{\mathrm{def}}{=} \underline{k} \otimes \boldsymbol{\nabla}$, are introduced. In addition, a dissipation potential $\phi(\underline{\dot{k}})$ is assumed, such that the dissipative stress is expressed as $\underline{\kappa}^{\mathrm{di}}(\underline{\dot{k}}) \stackrel{\mathrm{def}}{=} \partial\phi/\partial\underline{\dot{k}}$.

The strong formulation in primal format may be expressed as: Find the fields $\boldsymbol{u}(\boldsymbol{x}, t)$, $\underline{k}(\boldsymbol{x}, t)$ that satisfy:

$$-\boldsymbol{\sigma}(\boldsymbol{\epsilon}[\boldsymbol{u}], \underline{k}) \cdot \boldsymbol{\nabla} = \boldsymbol{0} \text{ in } \Omega \times \mathbb{R}^+, \tag{4.2}$$

$$\underline{\kappa}^{\mathrm{en}}(\boldsymbol{\epsilon}[\boldsymbol{u}], \underline{k}) + \underline{\kappa}^{\mathrm{di}}(\underline{\dot{k}}) - \underline{\boldsymbol{\xi}}(\underline{\boldsymbol{g}}[\underline{k}]) \cdot \boldsymbol{\nabla} = \underline{\boldsymbol{0}} \text{ in } \Omega \times \mathbb{R}^+, \tag{4.3}$$

and, the boundary conditions:

$$\boldsymbol{u} = \bar{\boldsymbol{u}}_{\mathrm{p}} \text{ on } \partial\Omega_{\mathrm{u}}, \tag{4.4}$$

$$\boldsymbol{t}[\boldsymbol{\sigma}] \stackrel{\text{def}}{=} \boldsymbol{\sigma} \cdot \boldsymbol{n} = \bar{\boldsymbol{t}}_{\mathrm{p}} \text{ on } \partial\Omega_{\mathrm{t}}, \tag{4.5}$$

$$\underline{p}[\underline{\boldsymbol{\xi}}] \stackrel{\text{def}}{=} \underline{\boldsymbol{\xi}} \cdot \boldsymbol{n} = \bar{\underline{\boldsymbol{p}}}_{\mathrm{p}} \text{ on } \partial\Omega_{\mathrm{p}}, \tag{4.6}$$

$$\underline{k} = \bar{\underline{k}}_{\mathrm{p}} \text{ on } \partial\Omega_{\mathrm{k}}. \tag{4.7}$$

Equation (4.2) is the standard equilibrium under quasi-static conditions (in the absence of volume forces), while Eq. (4.3) pertains to the "micro-force" balance equations, see e.g. Gurtin [43]. In Eqs. (4.2) and (4.3), the following variables have been introduced–in accordance with the Coleman-type equations:

$$\boldsymbol{\sigma} \stackrel{\text{def}}{=} \frac{\partial\psi}{\partial\boldsymbol{\epsilon}}, \quad \underline{\kappa}^{\mathrm{en}} \stackrel{\text{def}}{=} \frac{\partial\psi}{\partial\underline{k}}, \quad \underline{\boldsymbol{\xi}} \stackrel{\text{def}}{=} \frac{\partial\psi}{\partial\underline{\boldsymbol{g}}}. \tag{4.8}$$

In the strong formulation (4.2)–(4.7), emphasis should be given to the boundary conditions pertinent to the micro-force balance equations (4.3). Namely, either the micro-traction $\underline{p}$ ("free" boundary conditions), or, the internal variables $\underline{k}$ ("hard" boundary conditions) are prescribed on the relevant partitions of the surface $\partial\Omega$, see also Fig. 4.1. The choice of the aforementioned boundary conditions becomes particularly important in the comparison between the behavior of the gradient-enhanced formulation proposed here and a "standard" displacement-based formulation based on local constitutive theory. In the latter formulation, no such boundary conditions can be, nor need to be, prescribed.
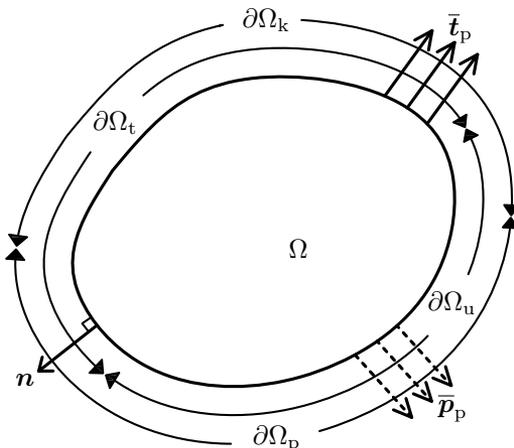
Figure 4.1: *Body occupying the domain Ω, surface tractions $\bar{\boldsymbol{t}}_{\mathrm{p}}$, micro-tractions $\bar{\underline{\boldsymbol{p}}}_{\mathrm{p}}$ and normal $\boldsymbol{n}$, and partitioning of the boundary into subdomains, $\partial\Omega = \partial\Omega_{\mathrm{u}} \cup \partial\Omega_{\mathrm{t}}$ and $\partial\Omega = \partial\Omega_{\mathrm{p}} \cup \partial\Omega_{\mathrm{k}}$.*

At the next step, two more independent fields are introduced in the considered strong formulation, namely $\underline{\kappa}^{\mathrm{di}}(\boldsymbol{x}, t)$ and $\underline{\boldsymbol{\xi}}(\boldsymbol{x}, t)$. For that purpose, the following Legendre

transformations are employed:

$$\phi^*(\underline{\kappa}^{\mathrm{di}}) = \sup_{\hat{\underline{k}}} \left[\underline{\kappa}^{\mathrm{di}} \star \hat{\underline{k}} - \phi(\hat{\underline{k}}) \right], \tag{4.9}$$

$$\varphi(\boldsymbol{\epsilon}, \underline{k}, \underline{\boldsymbol{\xi}}) = \inf_{\hat{\underline{\boldsymbol{g}}}} \left[\psi(\epsilon, k, \underline{\boldsymbol{g}}) - \underline{\boldsymbol{\xi}} \star \hat{\underline{\boldsymbol{g}}} \right]. \tag{4.10}$$

Thereby, the evolution rule for $\underline{k}$ is obtained from Eq. (4.9):

$$\dot{\underline{k}} = \frac{\partial \phi^*}{\partial \underline{\kappa}^{\mathrm{di}}}, \tag{4.11}$$

and, the constitutive equation for $\boldsymbol{g}(\underline{\boldsymbol{\xi}})$ is derived from Eq. (4.10):

$$\boldsymbol{g}(\underline{\boldsymbol{\xi}}) = -\frac{\partial \varphi}{\partial \underline{\boldsymbol{\xi}}}. \tag{4.12}$$

Including Eqs. (4.11) and (4.12), the time-discrete balance equations of the proposed *mixed-dual* format read: Find $\boldsymbol{u}(\boldsymbol{x})$, $\underline{\boldsymbol{\xi}}(\boldsymbol{x})$, $\underline{k}(\boldsymbol{x})$, $\underline{\kappa}^{\mathrm{di}}(\boldsymbol{x})$ that satisfy:

$$-\boldsymbol{\sigma}(\boldsymbol{\epsilon}[\boldsymbol{u}], \underline{k}) \cdot \boldsymbol{\nabla} = \boldsymbol{0} \quad \text{in} \ \ \Omega, \tag{4.13}$$

$$\underline{\kappa}^{\mathrm{en}}(\boldsymbol{\epsilon}[\boldsymbol{u}], \underline{k}) + \underline{\kappa}^{\mathrm{di}} - \underline{\boldsymbol{\xi}} \cdot \boldsymbol{\nabla} = \underline{\boldsymbol{0}} \quad \text{in} \ \ \Omega, \tag{4.14}$$

$$\boldsymbol{g}[\underline{k}] - \boldsymbol{g}(\underline{\boldsymbol{\xi}}) = \underline{\boldsymbol{0}} \quad \text{in} \ \ \Omega, \tag{4.15}$$

$$\underline{k} - \Delta t \frac{\partial \phi^*}{\partial \underline{\kappa}^{\mathrm{di}}}(\underline{\kappa}^{\mathrm{di}}) = {}^{n}\underline{k} \quad \text{in} \ \ \Omega, \tag{4.16}$$

where the Backward-Euler integration rule has been applied on Eqs. (4.13)–(4.16). In the time-discrete equations (4.13)–(4.16), the superindex $n+1$ is dropped for brevity.

Applying the principle of virtual work and Green-Gauss theorem, the *mixed-dual* variational format is obtained. Choosing to satisfy the variational formulation of Eqs. (4.14) and (4.16) in a strong sense (and eliminating $\underline{\kappa}^{\mathrm{di}}$), the global-local structure of the proposed *mixed-dual* variational formulation in terms of the residuals reads:

Global: Find $\boldsymbol{u}(\boldsymbol{x})$, $\underline{\boldsymbol{\xi}}(\boldsymbol{x})$, such that:

$$R_{\mathrm{u}}(\boldsymbol{u}, \underline{\boldsymbol{\xi}}; \delta\boldsymbol{u}) = \int_{\Omega} \boldsymbol{\sigma}(\boldsymbol{\epsilon}[\boldsymbol{u}], \underline{k}\{\boldsymbol{\epsilon}[\boldsymbol{u}], \underline{\boldsymbol{\chi}}[\underline{\boldsymbol{\xi}}]\}) : \boldsymbol{\epsilon}[\delta\boldsymbol{u}] \, \mathrm{d}\Omega - l^{(u)}(\delta\boldsymbol{u}) = 0, \tag{4.17}$$

$$R_{\underline{\boldsymbol{\xi}}}(\boldsymbol{u}, \underline{\boldsymbol{\xi}}; \delta\underline{\boldsymbol{\xi}}) = \int_{\Omega} \left[-\underline{k}\{\boldsymbol{\epsilon}[\boldsymbol{u}], \underline{\boldsymbol{\chi}}[\underline{\boldsymbol{\xi}}]\} \star \underline{\boldsymbol{\chi}}[\delta\underline{\boldsymbol{\xi}}] - \boldsymbol{g}(\underline{\boldsymbol{\xi}}) \star \delta\underline{\boldsymbol{\xi}} \right] \mathrm{d}\Omega - l^{(\underline{\xi})}(\delta\underline{\boldsymbol{\xi}}) = 0, \tag{4.18}$$

for suitable test functions $\delta\boldsymbol{u}$, $\delta\underline{\boldsymbol{\xi}}$, where $\underline{\boldsymbol{\chi}}[\underline{\boldsymbol{\xi}}] \stackrel{\mathrm{def}}{=} \underline{\boldsymbol{\xi}} \cdot \boldsymbol{\nabla}$.

Local: Find $\underline{k}(\boldsymbol{x})$, such that:

$$\underline{\boldsymbol{R}}_{\mathrm{L}}(\boldsymbol{u}, \underline{\boldsymbol{\xi}}, \underline{k}) = \underline{k} - \Delta t \frac{\partial \phi^*}{\partial \underline{\kappa}^{\mathrm{di}}}(\underline{\boldsymbol{\chi}}[\underline{\boldsymbol{\xi}}] - \underline{\kappa}^{\mathrm{en}}(\boldsymbol{\epsilon}[\boldsymbol{u}], \underline{k})) - {}^{n}\underline{k} = \underline{\boldsymbol{0}}, \tag{4.19}$$

for known values of $\boldsymbol{u}(\boldsymbol{x})$ and $\underline{\boldsymbol{\xi}}(\boldsymbol{x})$ (or else, of $\boldsymbol{\epsilon}[\boldsymbol{u}]$ and $\underline{\boldsymbol{\chi}}[\underline{\boldsymbol{\xi}}]$) at the integration points.

The boundary terms $l^{(u)}(\delta\boldsymbol{u})$ and $l^{(\underline{\xi})}(\delta\underline{\boldsymbol{\xi}})$ in Eqs. (4.17) and (4.18), read

$$l^{(u)}(\delta\boldsymbol{u}) = \int_{\partial\Omega_t} \bar{\boldsymbol{t}}_p \cdot \delta\boldsymbol{u}\,d\Gamma, \tag{4.20}$$

$$l^{(\underline{\xi})}(\delta\underline{\boldsymbol{\xi}}) = -\int_{\partial\Omega_k} \bar{\underline{\boldsymbol{k}}}_p \star \bar{\underline{\boldsymbol{p}}}[\delta\underline{\boldsymbol{\xi}}]\,d\Gamma. \tag{4.21}$$

The appropriate boundary conditions that need to be prescribed become apparent from the structure of the linear forms in Eqs. (4.20) and (4.21). The complete derivation of the proposed *mixed-dual* variational formulation is illustrated in Floros et al. [2], together with the discretization of the continuous system (4.17) and (4.18), and the nested iterations strategy for the solution of the resulting finite element and local equations.

4.3 Configurational motion problem

The thermodynamically consistent definition of the crack driving force based on material forces derived in Tillberg et al. [11] is adopted here. According to the latter work, the total configurational force $\boldsymbol{\mathcal{G}}$ is split into the configurational $\boldsymbol{\mathcal{G}}^{\mathrm{CONF}}$ and the material dissipation part $\boldsymbol{\mathcal{G}}^{\mathrm{MAT}}$. The respective forces in small strains setting for *local constitutive theory* read

$$\boldsymbol{\mathcal{G}}^{\mathrm{CONF}} = \int_\Omega -(\boldsymbol{\nabla}\overline{W}) \cdot \boldsymbol{\Sigma}\,d\Omega, \tag{4.22}$$

$$\boldsymbol{\mathcal{G}}^{\mathrm{MAT}} = \int_\Omega -\frac{\partial\psi}{\partial\underline{k}} \star [\underline{k} \otimes \boldsymbol{\nabla}]\overline{W}\,d\Omega, \tag{4.23}$$

where $\boldsymbol{\Sigma} \overset{\text{def}}{=} \psi\boldsymbol{I} - \boldsymbol{H}^{\mathrm{T}} \cdot \boldsymbol{\sigma}$ is the Eshelby energy momentum tensor, $\boldsymbol{H}(\boldsymbol{x},t) = [\boldsymbol{u} \otimes \boldsymbol{\nabla}]$, and $\overline{W}$ is a sufficiently smooth function that scales the configurational motion.

As regards *gradient-enhanced constitutive theory* adopted in Floros et al. [2], the material dissipation part takes the form

$$\boldsymbol{\mathcal{G}}^{\mathrm{MAT}} = \int_\Omega \left[-\underline{\boldsymbol{\kappa}}^{\mathrm{en}}(\epsilon, \underline{k}) \star \boldsymbol{g}(\underline{\boldsymbol{\xi}}) - \underline{\boldsymbol{\xi}} \star \left[\boldsymbol{g}(\underline{\boldsymbol{\xi}}) \otimes \boldsymbol{\nabla} \right] \right] \overline{W}\,d\Omega. \tag{4.24}$$

The advantage of the proposed *mixed-dual* variational formulation is clearly viewed in Eq. (4.24), where all the necessary quantities for the computation of $\boldsymbol{\mathcal{G}}^{\mathrm{MAT}}$ are known already from the solution of the primary problem. This is contrasted to the relevant expression for local theory Eq. (4.23). There, proper nodal smoothing of the internal variables from known values at the integration points is required at the post-processing.

For the illustrative examples that follow, a Bingham perfect viscoplastic material model is used, thereby $\underline{k} \equiv \boldsymbol{\epsilon}^{\mathrm{p}}$. The *semi-dual* free energy of the pertinent constitutive model for gradient-enhanced theory is expressed as:

$$\varphi(\boldsymbol{\epsilon}, \boldsymbol{\epsilon}^{\mathrm{p}}, \boldsymbol{\xi}) = \underbrace{\frac{1}{2}\left[\boldsymbol{\epsilon} - \boldsymbol{\epsilon}^{\mathrm{p}}\right] : \mathsf{E} : \left[\boldsymbol{\epsilon} - \boldsymbol{\epsilon}^{\mathrm{p}}\right]}_{\psi^{\mathrm{loc}}(\boldsymbol{\epsilon},\boldsymbol{\epsilon}^{\mathrm{p}})} - \underbrace{\frac{1}{2H_g l_s^2}|\boldsymbol{\xi}|^2}_{\psi^{*,\mathrm{gra}}(\boldsymbol{\xi})}, \tag{4.25}$$

where **E** is the fourth-order elasticity tensor, H_g may be viewed as a "gradient hardening" modulus, while l_s is an internal length scale, effectively acting here as a regularization parameter. The response of the proposed gradient-enhanced *mixed-dual* formulation as $l_s \to 0$ is of interest, and it is compared here to local theory based on a displacement-based variational formulation. For the latter formulation, a local Bingham perfect viscoplastic material is used, with the free energy $\psi = \psi^{loc}(\epsilon, \epsilon^p)$, whereas ψ^{loc} corresponds to the first term at the RHS of Eq. (4.25).

The computation of configurational forces is overviewed next, for the cases of a smooth interface (hole) and a discrete singularity (crack). The respective primary problems solved for are described in Figs. 4.2a and 4.2b. "Hard" boundary conditions, $\epsilon^p = \mathbf{0}$, or, "free" boundary conditions, $\boldsymbol{p} = \mathbf{0}$, are prescribed along the boundaries.
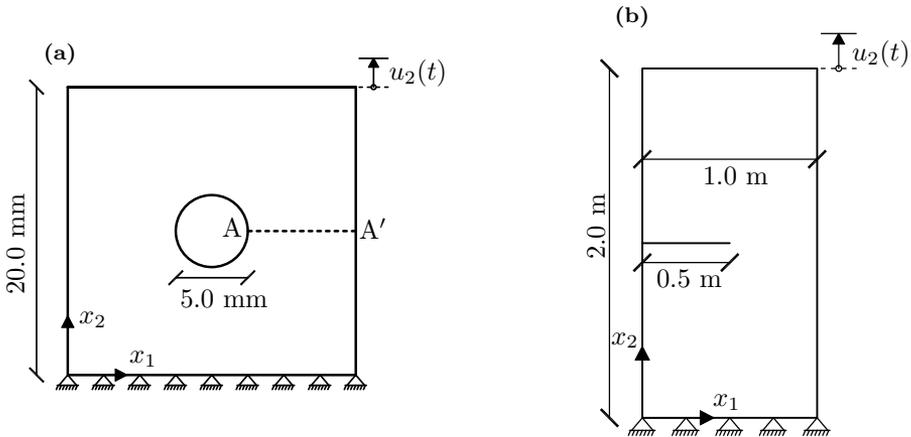
Figure 4.2: *Description of the primary problems solved for. (a) Plate with centric hole. (b) Single edge-cracked specimen.*

The considered configurational motions consist of a unit expansion of the hole and unit crack advance tangentially to the crack-tip, both scaled by function $\overline{W}$, see Figs. 4.3a and 4.3b. The mesh sensitivity of the energy release rate $\mathcal{G}$ is examined for the aforementioned configurational motions, which are computed based on the primary problems outlined in Figs. 4.2a and 4.2b. The energy release rate at a specific point is defined as the projection of the configurational force acting at that point onto the direction of configurational motion $\delta \boldsymbol{x}^1$, see Fig. 4.4a. This projection is commonly known as the *J*-integral for (non)linear elasticity (see Rice [39]), or else the component $\mathcal{G}_{\parallel}$ of the crack driving force, see Fig. 4.4b.

Results from the problem of the smooth interface are overviewed first. In Figs. 4.5 and 4.6, the respective parts, $\mathcal{G}^{CONF}$, and, $\mathcal{G}^{MAT}$, of the total energy release rate, $\mathcal{G}$, are illustrated, for varying values of the internal length scale l_s, for "hard" and "free" boundary conditions, respectively. In Fig. 4.6, the behavior of the local theory is approached as the internal length scale parameter tends to zero. This is not the case in Fig. 4.5, i.e. for

---

[1]The continuum mechanics setting for the configurational motion problem is described in detail in Floros et al. [2].
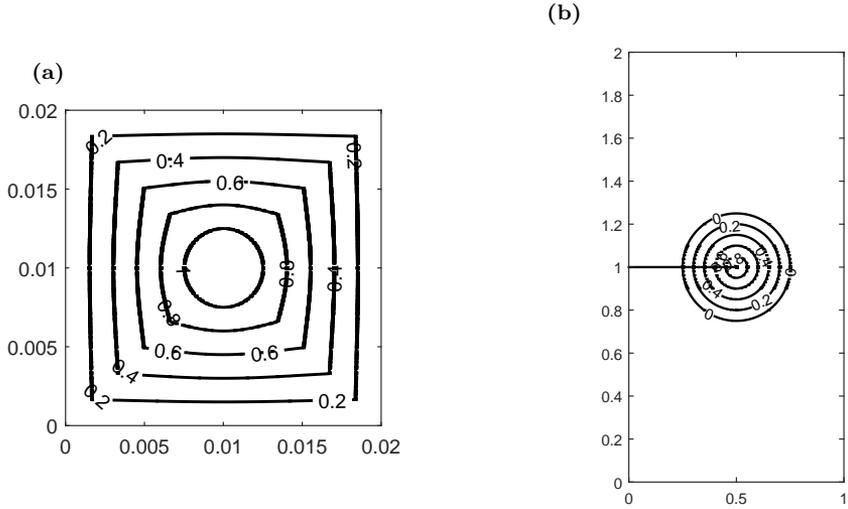
Figure 4.3: *Isolines denoting nodes that exhibit the same amount of configurational motion, over the integration domain of the configurational forces. The pertinent motion varies linearly from 1 at the inhomogeneity, to 0 at the boundary of the integration domain. (a) Plate with centric hole. (b) Single edge-cracked specimen.*
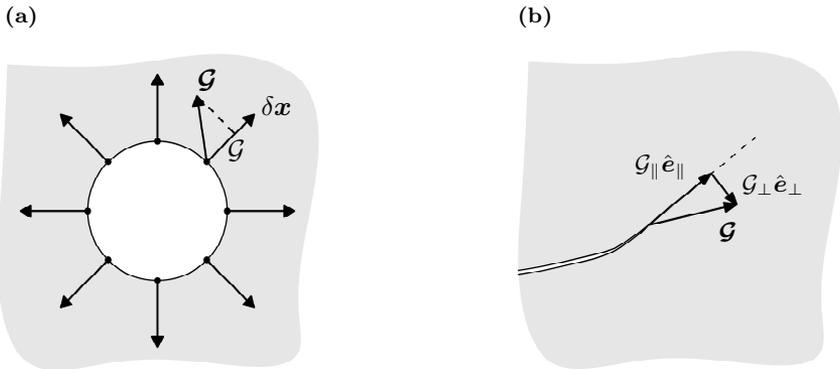
Figure 4.4: *Definitions related to the configurational motion problem. (a) Energy release rate $\mathcal{G}$. (b) Definition of tangential, $\mathcal{G}_{\parallel}$, and, perpendicular, $\mathcal{G}_{\perp}$, component of CDF, $\boldsymbol{\mathcal{G}}$.*

"hard" boundary conditions. The difference in the observed behavior depending on the choice of boundary conditions is explained in Floros et al. [2].

The corresponding parts of the total energy release rate for the single edge-cracked specimen for varying values of the internal length scale l_{s}, for "hard" boundary conditions, $\boldsymbol{\epsilon}^{\mathrm{p}} = \mathbf{0}$, are shown in Fig. 4.7. It is observed that the behavior of the local theory is approached as the internal length scale parameter tends to zero. The same holds for "free" boundary conditions, $\boldsymbol{p} = \mathbf{0}$ (see Floros et al. [2]). The convergence of the relative error in
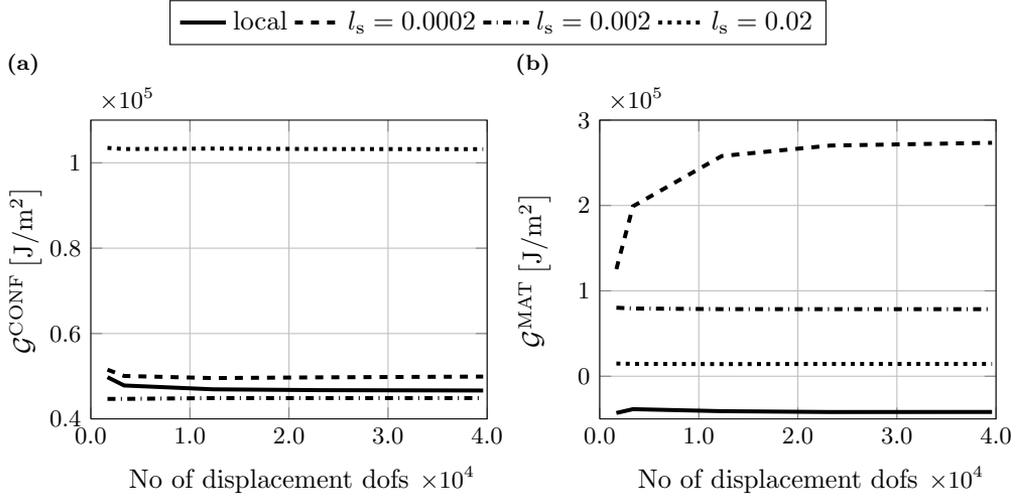
Figure 4.5: *Energy release rates obtained via local and gradient-enhanced constitutive theory. Case of "hard" boundary conditions, $\boldsymbol{\epsilon}^{\mathrm{p}} = \mathbf{0}$. (a) $\mathcal{G}^{\mathrm{CONF}}$. (b) $\mathcal{G}^{\mathrm{MAT}}$.*
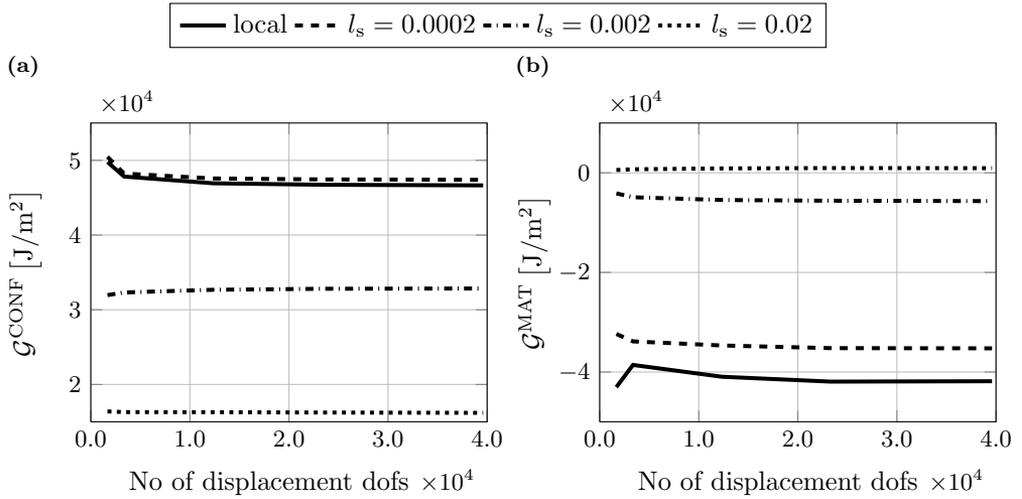
Figure 4.6: *Energy release rates obtained via local and gradient-enhanced constitutive theory. Case of "free" boundary conditions, $\boldsymbol{p} = \mathbf{0}$. (a) $\mathcal{G}^{\mathrm{CONF}}$. (b) $\mathcal{G}^{\mathrm{MAT}}$.*

$\mathcal{G}^{\mathrm{MAT}}$ for "hard" boundary conditions and the variation of $\mathcal{G}_{\parallel}$ with respect to the length scale are shown in Fig. 4.8.
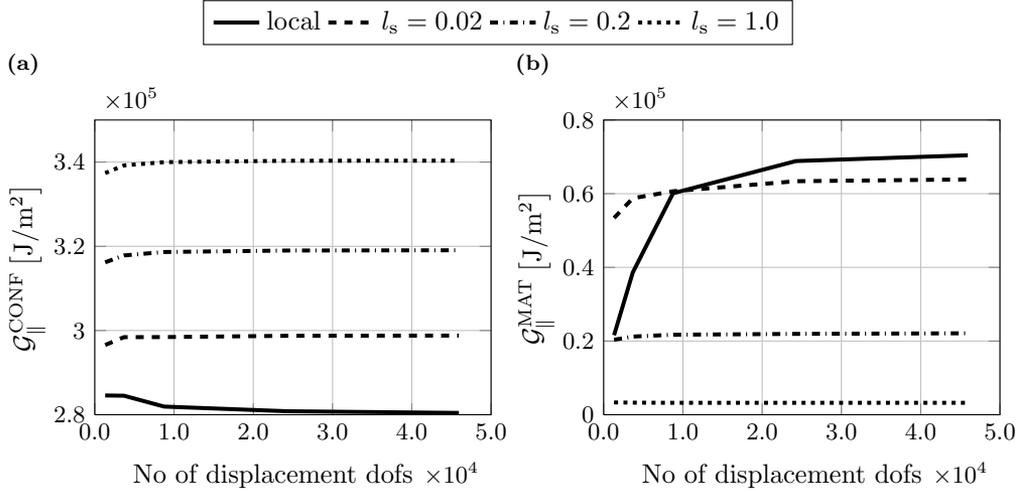
Figure 4.7: *Energy release rates at the last incremental loading step, obtained via local and gradient-enhanced constitutive theory. Case of "hard" boundary conditions, $\boldsymbol{\epsilon}^{\mathrm{p}} = \mathbf{0}$. (a) $\mathcal{G}_{\parallel}^{\mathrm{CONF}}$. (b) $\mathcal{G}_{\parallel}^{\mathrm{MAT}}$.*
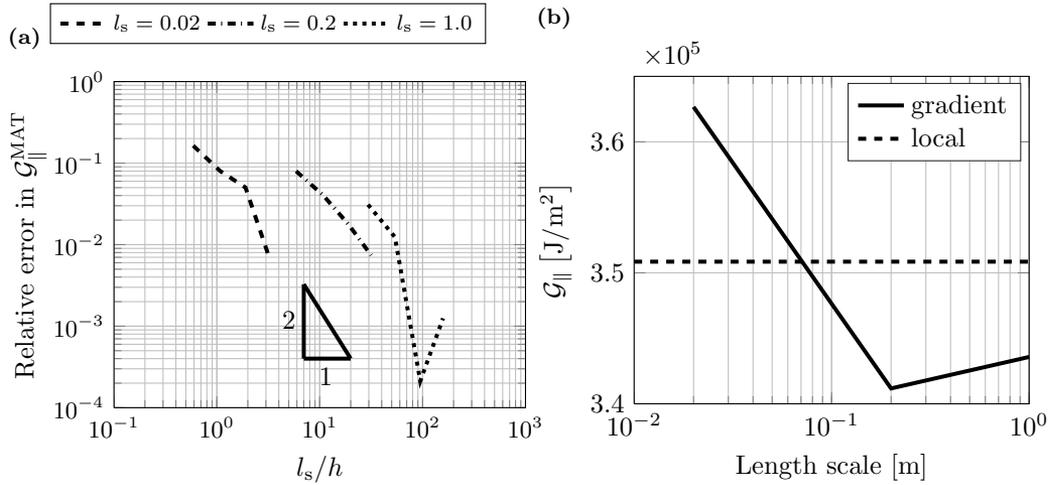
Figure 4.8: *(a) Convergence of the relative error in $\mathcal{G}_{\parallel}^{\mathrm{MAT}}$ for "hard" boundary conditions, $\boldsymbol{\epsilon}^{\mathrm{p}} = \mathbf{0}$. (b) Variation of $\mathcal{G}_{\parallel}$ with respect to the length scale parameter, for "hard" boundary conditions, $\boldsymbol{\epsilon}^{\mathrm{p}} = \mathbf{0}$.*

5 Future work

5.1 Effect of crack face friction under pronounced crack closure conditions

In Floros et al. [1], the effect of combined alternating axial and static or cyclic torsion on the elastic–plastic deformation of cracks is studied. In order to limit the influencing factors in this study, friction-less contact is assumed between the crack faces. The simulations are performed on pre-cracked thin-walled tubular specimens, thereby the influence of crack face friction would be limited even if it would have been taken into account. In addition, the applied loading features mainly "growth" under tensile conditions, whereas RCF crack propagation takes place primarily under mixed mode II & III, under substantial compression. Under these conditions, it is expected that crack face friction has a significant effect on crack propagation, see also Lansler and Kabo [48], Bogdański and Brown [33]. In the general case, the large compressive stresses imposed by passing wheels interact with factors such as particle interlocking, which complicates a detailed study of frictional effects even further.

The role of crack face friction on crack loading, as measured by crack face displacements is scheduled for a future investigation. In order to allow for substantial frictional effects to develop at the crack faces, the study should be performed on thick-walled FE-models (cf. thin-walled FE-models in Floros et al. [1]), under primary cyclic compressive and torsional load combinations.

5.2 Computation of configurational forces for inelasticity

In Floros et al. [2], a gradient-enhanced *mixed-dual* variational formulation is developed. An internal length scale is used as a regularization parameter. The configurational forces field computed based on this formulation is found to be a computable quantity. Regularization enters in two ways in the aforementioned work. Namely, via the gradient-effects accounted in the free energy, as well as by employing a (perfect) viscoplastic material model. In the same work, the "limit" case of local constitutive theory is examined for decreasing values of the internal length scale. Another limit case worth investigating comprises the case of rate-independent plasticity (elastoplasticity), i.e. tuning the viscoplastic time parameter(s) in a way that results, essentially, in a rate-independent material response. Provided that the latter scheme results in computable material forces, yields the inclusion of gradient-effects in the free energy as a major regularization factor for the proposed *mixed-dual* variational formulation in Floros et al. [2].

As an outlook on the field of configurational forces for inelasticity, more topics still require further investigation. In the majority of the published work in literature on the topic, the definition used for the material forces stems from either the balance of a so-called pseudomomentum (see e.g. Steinmann [41]), or as a variational "construct" from

the partial variation of the total mechanical dissipation, see e.g. Tillberg et al. [11]. Thus, there exists minimal work towards the establishment of a potential for the specific problem at hand. In turn, stationarity of that potential would yield the quantities that minimize the potential *ab initio* computable (in theory). Similarly, it is still not well-established how to properly include surface tractions in configurational motion problems of singularities, even in the case of hyperelasticity, see Brouzoulis and Ekh [8].

6   Summary of appended papers

6.1   Paper A: A numerical investigation of elastoplastic deformation of cracks in tubular specimens subjected to combined torsional and axial loading

A numerical investigation is performed on pre-cracked tubular specimens under combined alternating and/or static axial and torsional loading in various load configurations. The elastic–plastic deformation of the crack faces is quantified via crack face displacements. The range of the crack face displacements over each load cycle effectively serves as an indicator of the severity of the crack loading. Identified *ratcheting* effects in crack face displacements are linked to *crack blunting*, while *shakedown* effects indicate the build-up of residual stresses. Obtained numerical results are linked to experimental trends in literature.

6.2   Paper B: On configurational forces for gradient-enhanced inelasticity

Configurational (or material) forces are computed within a gradient-enhanced constitutive theory, based on a mixed variational formulation. The mixed formulation consists of the displacements along with the stress measure which is energy conjugated to the spatial gradient of the internal variables. An internal length scale measure is used as a regularization parameter.

The mesh sensitivity of the energy release rates pertinent to the computed material forces is examined for the case of a smooth interface and a discrete singularity. Results showcase that the proposed gradient-enhanced mixed formulation provides sufficient regularity for the computation of material forces. The relative error of convergence is shown to decrease quadratically or higher with respect to the ratio of the internal length scale to the characteristic element size.

References

[1] D. Floros, A. Ekberg, and K. Runesson. A numerical investigation of elastoplastic deformation of cracks in tubular specimens subjected to combined torsional and axial loading. *International Journal of Fatigue* (2016). ISSN: 0142-1123.

[2] D. Floros, F. Larsson, and K. Runesson. On configurational forces for gradient-enhanced inelasticity. *To be submitted for international publication* (2016).

[3] M. Marshall, R Lewis, R. Dwyer-Joyce, U. Olofsson, and S. Björklund. Experimental characterization of wheel-rail contact patch evolution. *Journal of tribology* **128**.3 (2006), 493–504.

[4] G. Girsch, J. Keichel, R. Gehrmann, A. Zlatnik, and N. Frank. "Advanced rail steels for heavy haul applications–track performance and weldability". *IHHA conference, Shanghai*. 2009.

[5] E. E. Magel. *Rolling contact fatigue: a comprehensive review*. Tech. rep. 2011.

[6] N. E. Dowling. *Mechanical behavior of materials: engineering methods for deformation, fracture, and fatigue*. Prentice hall, 1993. ISBN: 0135790468.

[7] K. Tanaka. Fatigue crack propagation from a crack inclined to the cyclic tensile axis. *Engineering Fracture Mechanics* **6**.3 (1974), 493–507. ISSN: 0013-7944.

[8] J. Brouzoulis and M. Ekh. Crack propagation in rails under rolling contact fatigue loading conditions based on material forces. *International Journal of Fatigue* **45** (2012), 98–105. ISSN: 0142-1123.

[9] A. A. Griffith. The phenomena of rupture and flow in solids. *Philosophical transactions of the royal society of london. Series A, containing papers of a mathematical or physical character* **221** (1921), 163–198. ISSN: 0264-3952.

[10] B. Näser, M. Kaliske, and R. Müller. Material forces for inelastic models at large strains: application to fracture mechanics. *Computational Mechanics* **40**.6 (2007), 1005–1013. ISSN: 0178-7675.

[11] J. Tillberg, F. Larsson, and K. Runesson. On the role of material dissipation for the crack-driving force. *International Journal of Plasticity* **26**.7 (2010), 992–1012. ISSN: 0749-6419.

[12] K. Runesson, F. Larsson, and P. Steinmann. On energetic changes due to configurational motion of standard continua. *International Journal of Solids and Structures* **46**.6 (2009), 1464–1475. ISSN: 0020-7683.

[13] N. Larijani, J. Brouzoulis, M. Schilke, and M. Ekh. The effect of anisotropy on crack propagation in pearlitic rail steel. *Wear* **314**.1 (2014), 57–68. ISSN: 0043-1648.

[14] A. F. Bower. The Influence of Crack Face Friction and Trapped Fluid on Surface Initiated Rolling Contact Fatigue Cracks. *Journal of Tribology* **110**.4 (1988), 704–711. ISSN: 0742-4787. DOI: 10.1115/1.3261717.

[15] M Fonte and M De Freitas. Marine main engine crankshaft failure analysis: a case study. *Engineering Failure Analysis* **16**.6 (2009), 1940–1947. ISSN: 1350-6307.

[16] I. V. Papadopoulos. Exploring the high-cycle fatigue behaviour of metals from the mesoscopic scale. *Journal of the Mechanical Behavior of Materials* **6**.2 (1996), 93–118. ISSN: 2191-0243.

[17] A. Fatemi and N. Shamsaei. Multiaxial fatigue: An overview and some approximation models for life estimation. *International Journal of Fatigue* **33**.8 (2011), 948–958. ISSN: 0142-1123.

[18] M Fonte, L Reis, F Romeiro, B Li, and M Freitas. The effect of steady torsion on fatigue crack growth in shafts. *International journal of fatigue* **28**.5 (2006), 609–617. ISSN: 0142-1123.

[19] M De Freitas, L Reis, M Da Fonte, and B Li. Effect of steady torsion on fatigue crack initiation and propagation under rotating bending: Multiaxial fatigue and mixed-mode cracking. *Engineering Fracture Mechanics* **78**.5 (2011), 826–835.

[20] F. Yang, Z. Kuang, and V. Shlyannikov. Fatigue crack growth for straight-fronted edge crack in a round bar. *International journal of fatigue* **28**.4 (2006), 431–437. ISSN: 0142-1123.

[21] M. Brown, E Hay, and K. Miller. Fatigue at notches subjected to reversed torsion and static axial loads. *Fatigue & Fracture of Engineering Materials & Structures* **8**.3 (1985), 243–258. ISSN: 1460-2695.

[22] F Hourlier and A Pineau. Propagation of fatigue cracks under polymodal loading. *Fatigue & Fracture of Engineering Materials & Structures* **5**.4 (1982), 287–302. ISSN: 1460-2695.

[23] H. Zhizhong, M. Lihua, and C. Shuzhen. A study of shear fatigue crack mechanisms. *Fatigue & Fracture of Engineering Materials & Structures* **15**.6 (1992), 563–572. ISSN: 1460-2695.

[24] E. Tschegg, S. Stanzl, H. Mayer, and M Czegley. Crack face interactions and near-threshold fatigue crack growth. *Fatigue & Fracture of Engineering Materials & Structures* **16**.1 (1993), 71–83. ISSN: 1460-2695.

[25] R. Ritchie, F. McClintock, H Nayeb-Hashemi, and M. Ritter. Mode III fatigue crack propagation in low alloy steel. *Metallurgical Transactions A* **13**.1 (1982), 101–110. ISSN: 0360-2133.

[26] E. Tschegg and S. Stanzl. The significance of sliding mode crack closure on mode III fatigue crack growth. *Basic Questions in Fatigue.* **1** (1984), 214–232.

[27] A. Ekberg and E. Kabo. Fatigue of railway wheels and rails under rolling contact and thermal loading—an overview. *Wear* **258**.7–8 (2005), 1288–1300. ISSN: 0043-1648. DOI: http://dx.doi.org/10.1016/j.wear.2004.03.039.

[28] J. W. Ringsberg and A. Bergkvist. On propagation of short rolling contact fatigue cracks. *Fatigue & Fracture of Engineering Materials & Structures* **26**.10 (2003), 969–983. ISSN: 1460-2695.

[29] F. Erdogan and G. Sih. On the crack extension in plates under plane loading and transverse shear. *Journal of basic engineering* **85**.4 (1963), 519–525. ISSN: 0021-9223.

[30] A Otsuka, K Mori, S TSUYAMA, and T OHSHIMA. Fatigue crack growth of steel and aluminum alloy specimens under mode II loading. *Japan Society of Materials Science, Journal* **29** (1980), 1042–1048.

[31] P. Bold, M. Brown, and R. Allen. Shear mode crack growth and rolling contact fatigue. *Wear* **144**.1-2 (1991), 307–317. ISSN: 0043-1648.

[32] S. Wong, P. Bold, M. Brown, and R. Allen. A branch criterion for shallow angled rolling contact fatigue cracks in rails. *Wear* **191**.1 (1996), 45–53. ISSN: 0043-1648.

[33] S. Bogdański and M. W. Brown. Modelling the three-dimensional behaviour of shallow rolling contact fatigue cracks in rails. *Wear* **253**.1–2 (2002), 17–25. ISSN: 0043-1648. DOI: `http://dx.doi.org/10.1016/S0043-1648(02)00078-9`.

[34] G. C. Sih. Strain-energy-density factor applied to mixed mode crack problems. *International Journal of fracture* **10**.3 (1974), 305–321. ISSN: 0376-9429.

[35] C.-H. Chue and H. Chung. Pitting formation under rolling contact. *Theoretical and applied fracture mechanics* **34**.1 (2000), 1–9. ISSN: 0167-8442.

[36] E. Tschegg. The influence of the static I load mode and R ratio on mode III fatigue crack growth behaviour in mild steel. *Materials Science and Engineering* **59**.1 (1983), 127–137. ISSN: 0025-5416.

[37] S. Suresh. *Fatigue of materials*. Cambridge university press, 1998. ISBN: 0521578477.

[38] C. Li. Vector CTD criterion applied to mixed mode fatigue crack growth. *Fatigue & Fracture of Engineering Materials & Structures* **12**.1 (1989), 59–65. ISSN: 1460-2695.

[39] J. R. Rice. *A path independent integral and the approximate analysis of strain concentration by notches and cracks*. Report. DTIC Document, 1967.

[40] T Hoshide and D. Socie. Mechanics of mixed mode small fatigue crack growth. *Engineering Fracture Mechanics* **26**.6 (1987), 841–850. ISSN: 0013-7944.

[41] P. Steinmann. Application of material forces to hyperelastostatic fracture mechanics. I. Continuum mechanical setting. *International Journal of Solids and Structures* **37**.48 (2000), 7371–7391. ISSN: 0020-7683.

[42] A. Menzel, R. Denzer, and P. Steinmann. On the comparison of two approaches to compute material forces for inelastic materials. Application to single-slip crystal-plasticity. *Computer methods in applied mechanics and engineering* **193**.48 (2004), 5411–5428. ISSN: 0045-7825.

[43] M. E. Gurtin. A gradient theory of single-crystal viscoplasticity that accounts for geometrically necessary dislocations. *Journal of the Mechanics and Physics of Solids* **50**.1 (2002), 5–32. ISSN: 0022-5096.

[44] M. da Fonte and M. de Freitas. Stress intensity factors for semi-elliptical surface cracks in round bars under bending and torsion. *International Journal of Fatigue* **21**.5 (1999), 457–463. ISSN: 0142-1123.

[45] R Citarella, M Lepore, V Shlyannikov, and R Yarullin. Fatigue surface crack growth in cylindrical specimen under combined loading. *Engineering Fracture Mechanics* **131** (2014), 439–453. ISSN: 0013-7944.

[46] Y. Xu and H. Yuan. On damage accumulations in the cyclic cohesive zone model for XFEM analysis of mixed-mode fatigue crack growth. *Computational Materials Science* **46**.3 (2009), 579–585. ISSN: 0927-0256.

[47] Abaqus. Version 6.13 Documentation (Abaqus). *Abaqus user's guide* (2013).

[48] E. Lansler and E. Kabo. Subsurface crack face displacements in railway wheels. *Wear* **258**.7 (2005), 1038–1047. ISSN: 0043-1648.

[49] G. Hua, M. Brown, and K. Miller. Mixed-mode fatigue thresholds. *Fatigue & Fracture of Engineering Materials & Structures* **5**.1 (1982), 1–17. ISSN: 1460-2695.

[50] M. A. Sutton, X. Deng, F. Ma, J. C. Newman Jr, and M. James. Development and application of a crack tip opening displacement-based mixed mode fracture criterion. *International Journal of Solids and Structures* **37**.26 (2000), 3591–3618. ISSN: 0020-7683.